

# JGR Space Physics

## RESEARCH ARTICLE

10.1029/2018JA025995

### Key Points:

- Two days with similar heights of post-sunset equatorial F layer base have different latitudinal distributions of VHF and L-band scintillations
- Estimated densities of thermospheric O on these 2 days using CTIpe model show enhancement on the day preceded by a magnetic storm
- Enhanced ion-neutral collision frequency on this day limits vertical extent of EPB, which impacts latitudinal distribution of scintillations

### Correspondence to:

A. Bhattacharyya,  
abh@iigs.res.in

### Citation:

Bhattacharyya, A., Fedrizzi, M., Fuller-Rowell, T. J., Gurram, P., Kakad, B., Sripathi, S., & Sunda, S. (2019). Effect of magnetic storm related thermospheric changes on the evolution of equatorial plasma bubbles. *Journal of Geophysical Research: Space Physics*, 124, 2256–2270. <https://doi.org/10.1029/2018JA025995>

Received 14 AUG 2018






Accepted 21 FEB 2019

Accepted article online 24 FEB 2019

Published online 25 MAR 2019

©2019. American Geophysical Union.  
All Rights Reserved.

## Effect of Magnetic Storm Related Thermospheric Changes on the Evolution of Equatorial Plasma Bubbles

A. Bhattacharyya<sup>1</sup> , M. Fedrizzi<sup>2</sup> , T. J. Fuller-Rowell<sup>2</sup>, P. Gurram<sup>1</sup>, B. Kakad<sup>1</sup> , S. Sripathi<sup>1</sup> , and S. Sunda<sup>3</sup> 

<sup>1</sup>Indian Institute of Geomagnetism, Navi Mumbai, India, <sup>2</sup>CIRES, University of Colorado, Boulder, CO, USA, <sup>3</sup>Space Application Centre, Ahmedabad, India

**Abstract** Past efforts to predict scintillations on VHF and L-band radio signals recorded at equatorial and low-latitude stations have been mostly based on a theoretical linear growth rate of Rayleigh-Taylor instability on the bottomside of the post-sunset equatorial F layer, which is responsible for the generation of an equatorial plasma bubble (EPB). However, it is the maximum height that an EPB reaches above the dip equator and development of intermediate scale irregularities within the EPB, in its nonlinear phase of evolution that determines the latitudinal distribution of scintillations. Amplitude scintillations recorded by a network of VHF and L-band receivers on a quiet day, 13 March 2015 and on 20 March 2015, a few days after the 17 March 2015 magnetic storm, show that latitudinal extent of scintillations caused by EPB irregularities is lesser on 20 March than on 13 March. Geomagnetic and ionosonde data from an equatorial station, and vertical total electron content distributions obtained from Global Navigation Satellite Systems observations, indicate that the equatorial ionospheric conditions are approximately same on these 2 days. Simulation of thermospheric conditions for these 2 days is carried out using the Coupled Thermosphere, Ionosphere, Plasmasphere, and Electrodynamics model. It is found that thermospheric atomic oxygen density is enhanced in the aftermath of the major magnetic storm of 17 March 2015, resulting in enhanced ion-neutral collision frequencies over the dip equator on 20 March. This limits the height to which an EPB rises over the dip equator on this day, and thus impacts the latitudinal distribution of scintillations.

### 1. Introduction

There have been numerous studies in the last two decades, based on satellite and ground-based observations using a variety of instruments, on the effects of geomagnetic activity on the occurrence of the equatorial plasma bubble (EPB) in the nighttime equatorial and low-latitude ionosphere (Abdu, 2012; Abdu et al., 2003; Basu et al., 2007, 2010; Bhattacharyya et al., 2002; Chakrabarty et al., 2006; Kakad et al., 2007; Li et al., 2010; Martinis et al., 2005; Tulasi Ram et al., 2008). The EPB phenomenon, which arises due to the growth of the Rayleigh-Taylor (R-T) instability on the bottomside of the nighttime equatorial F layer, owes its importance to the fact that in the nonlinear stage of development of the R-T instability, the plasma depleted EPB not only rises to the otherwise linearly stable topside of the equatorial ionosphere, but also smaller scale structures develop in the EPBs, which are capable of scattering incident radio waves of VHF and higher frequencies. This has ramifications for radio signals routinely used for communication and navigation and may lead to significant degradation of the operation of satellite-based navigation systems such as the Global Navigation Satellite Systems (GNSS). The R-T instability involves the interchange of magnetic flux tubes and therefore it grows only when the conjugate E-region conductivities at the feet of the geomagnetic field lines connecting them to the equatorial F region are low enough to allow the interchange (Bhattacharyya, 2004). Otherwise, the perturbation electric fields associated with the R-T instability, which map down to these conjugate E-regions, are shorted out by currents that flow through the conducting E-regions, and the R-T instability cannot grow. Thus, the EPB is basically a nighttime phenomenon. The structures that develop within the EPB on the topside equatorial ionosphere map down along the geomagnetic field lines to off-equatorial latitudes, where they may cause considerable fluctuations or scintillations in the amplitude and phase of incident radio waves. In fact it is well known that scintillations on L-band signals recorded near the crest of the equatorial ionization anomaly region are stronger than on those recorded near the dip equator (Bhattacharyya et al., 2003, 2017; Groves et al., 1997; Mullen et al., 1985; Sripathi et al., 2008). Hence, there are two important aspects of the development of EPBs which impact the latitudinal distribution of the strength of scintillations on VHF and higher frequency trans-ionospheric radio signals: (a) maximum

height to which an EPB rises over the dip equator; (b) development of intermediate scale (~100 m to few kilometers) irregularities within an EPB. Both of these factors arise during the nonlinear phase of growth of the R-T instability.

Some of the references listed in the beginning of the previous paragraph are concerned with identifying the longitude interval where low-latitude ionospheric irregularities occur during the main phase of magnetic storms. The authors explain such occurrence of irregularities on the basis of the prompt penetration of an eastward electric field into the post-sunset equatorial ionosphere. This causes an additional height rise of the equatorial F layer over that expected due to the quiet time pre-reversal enhancement (PRE) of the post-sunset equatorial eastward electric field. In order to accomplish this, Basu et al. (2007, 2010) have used the rate of decrease of Dst index or the SYM-H index to identify longitude regions where the dusk sector coincides with rapid decrease in these indices for storms that are fairly large as indicated by the minimum values reached by these indices. Martinis et al. (2005) have investigated the possibilities of onset as well as suppression of the growth of the R-T instability during magnetically disturbed periods by using the Fejer-Scherliess empirical model (Fejer, 2002; Fejer & Scherliess, 1997) for disturbance vertical drifts in the equatorial ionosphere as a function of storm time and local time, based on storm time variation of AE index. Thus, the effects of disturbance dynamo electric fields (DDEFs) were also considered by Martinis et al. (2005), who showed that in some cases, presence of westward DDEFs in the dusk sector lead to the suppression of the growth of the R-T instability and hence the development of equatorial spread F (ESF) as seen in ionosonde data. On the other hand, occurrence of equatorial ionospheric irregularities during magnetically disturbed post-midnight periods have often been attributed to the presence of eastward DDEF (Li et al., 2010; Martinis et al., 2005). However, before attributing these post-midnight irregularities to eastward DDEF or eastward promptly penetrated electric fields (PPEFs), it has to be ensured that these irregularities are freshly generated over that location and are not fossil irregularities, which were generated earlier at another longitude and then drifted to the location being studied along with the ambient plasma. A method was developed by Bhattacharyya et al. (2002), based on spaced receiver scintillation data, to distinguish between nascent and fossil irregularities observed after 22 hr local time (LT), and this technique was used by Kakad et al. (2007) to identify nascent irregularities which were generated after 22 LT due to the presence of eastward DDEF or PPEF during magnetically disturbed periods.

In all the aforementioned studies, the emphasis on the presence of an eastward electric field is because of the key role played by the height of the bottomside equatorial F layer in the occurrence of EPBs as indicated by a linear theory of the R-T instability (Fejer et al., 1999; Sultan, 1996). In a more recent study (Carter, Yizengaw, et al., 2014), the flux tube-integrated linear growth rate of the R-T instability has been estimated by using the National Center for Atmospheric Research Thermosphere-Ionosphere-Electrodynamics General Circulation Model (TIEGCM) driven by the solar F10.7 index and the Kp index, in order to explain the day-to-day variability in the occurrence of EPBs due to changing ambient conditions. In another study, these authors (Carter, Retterer, Yizengaw, Groves, et al., 2014) used Kp values based on solar wind data to drive TIEGCM, in an effort to forecast the occurrence of L-band scintillations at some low-latitude stations in the African and Asian longitude sectors. However, these studies based on the linear growth rate of the R-T instability cannot account for the occurrence or nonoccurrence of scintillations at off-equatorial locations that require the EPB to rise to a specific height over the dip equator and develop intermediate scale size irregularities, which happen only in the nonlinear phase of growth of the R-T instability. It is therefore necessary to study the role that ambient conditions play in these aspects of the development of an EPB. In this paper, VHF and L-band scintillations recorded by a network of equatorial and low-latitude stations in the Indian longitude zone are used together with ionosonde and geomagnetic data to study the variations in the nonlinear evolution of EPBs in the days immediately following a major magnetic storm. Comparison of the ambient plasma conditions with that prevailing on a geomagnetically quiet day before the storm indicates a role played by the ambient thermosphere in the nonlinear evolution of EPBs, which needs to be taken into account to explain the day-to-day variability of the latitudinal distribution of L-band scintillations on the days that EPBs occur.

## 2. Ionosonde and Geomagnetic Observations at Equatorial Station

Global ionospheric effects of the geomagnetic storm on 17 March 2015 have emerged as the most extensively studied magnetic storm effects in recent years (Carter et al., 2016; Huang et al., 2016; Jiang et al., 2017; Kakad

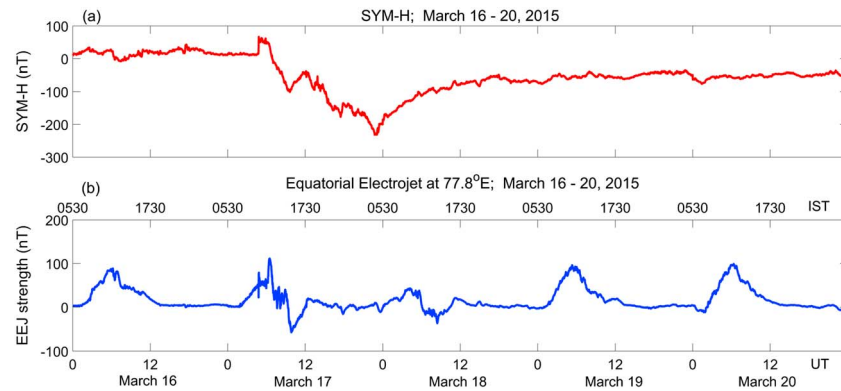


**Figure 1.** (a) Temporal variation of SYM-H during 16–20 March 2015. (b) Temporal variation of the strength of the EEJ in the Indian longitude region during 16–20 March 2015. EEJ = equatorial electrojet.

et al., 2016; Kil et al., 2016; Kuai et al., 2016; Nava et al., 2016; Nayak et al., 2016; Ramsingh et al., 2015; Ray et al., 2017; Tulasi Ram et al., 2016; Zhou et al., 2016). As has been recorded in several of the above references, and shown here in Figure 1a, on 17 March 2015, following a sudden storm commencement triggered at about 04:45 UT, the SYM-H index started decreasing when the z-component of the interplanetary magnetic field (IMF) turned southward at ~6 UT, indicating the onset of the magnetic storm. Intensification of the ring current caused SYM-H to decrease to a value of about  $-100$  nT, before starting a brief recovery when the IMF  $B_z$  turned northward around 09:30 UT. At about 12:30 UT, IMF  $B_z$  again turned southward, and remained mostly southward for nearly 11 hr causing the ring current to strengthen and SYM-H to reach a minimum value of  $-232$  nT at 23:04 UT, after which the recovery phase of the storm started (Nayak et al., 2016; Tulasi Ram et al., 2016). As the goal of the present paper is to study the evolution of EPBs well into the recovery phase of a major geomagnetic storm, condition of the equatorial ionosphere in the Indian longitude zone is monitored through the period 16–20 March 2015. During daytime, strength of the equatorial electrojet (EEJ) is estimated from the difference  $\Delta H$  in the horizontal components of the geomagnetic field variations from the night time values, recorded at an equatorial station and an off-equatorial station. EEJ strength provides information about the zonal electric field present in the equatorial E region during magnetically quiet as well as disturbed times (Anderson et al., 2002; Anghel et al., 2007; Rastogi & Klobuchar, 1990). In this study, geomagnetic data from the equatorial station Tirunelveli ( $8.7^\circ\text{N}$ ,  $77.8^\circ\text{E}$ , geomagnetic latitude  $0.2^\circ\text{N}$ ) and off-equatorial station Alibag ( $18.6^\circ\text{N}$ ,  $72.9^\circ\text{E}$ , geomagnetic latitude  $10^\circ\text{N}$ ) have been used for computation of EEJ strength. Figure 1b shows how the EEJ in the Indian longitude region has varied through the period 16–20 March 2015. Indian Standard Time (IST) is equal to UT + 5.5 hr. The 16 March 2015 was a magnetically quiet day. On 17 March, there is a short-lived increase in EEJ strength at 6 UT, the time of onset of the geomagnetic storm, which may be due to the prompt penetration of an eastward electric field into the daytime equatorial ionosphere due to the southward turning of IMF  $B_z$ . At the time of northward turning of IMF  $B_z$  around 09:30 UT, an overshielding westward electric field promptly penetrated into the equatorial ionosphere in the Indian sector, to produce a significant counter-electrojet. At this time an eastward PPEF was reported in the American sector where the local time was pre-sunrise (Nayak et al., 2016). EEJ does not provide any information about the equatorial zonal electric field in the post-sunset hours when the E-region conductivity is very low. However, it shows the presence of a strong DDEF, which is westward during the daytime hours of 18 March, when IMF  $B_z$  is northward, and no PPEF is present. Generally, DDEF is weaker in the daytime than at nighttime (Fejer, 2002; Fejer & Scherliess, 1997; Scherliess & Fejer, 1997). On 19 March, any DDEF that may be present during daytime is sufficiently weak so that the EEJ has recovered its quiet time pattern of daily variation, which also seems to be the case on 20 March 2015. This weakening of DDEF is also seen in the results for the Asian sector presented by Nava et al. (2016) for the days following the 17 March 2015 storm.

The equatorial station, Tirunelveli (TIR) is equipped with a Canadian Advanced Digital Ionosonde (CADI), which has provided ionograms for estimating F region virtual height h'F. In Figure 2, h'F between 1800 IST

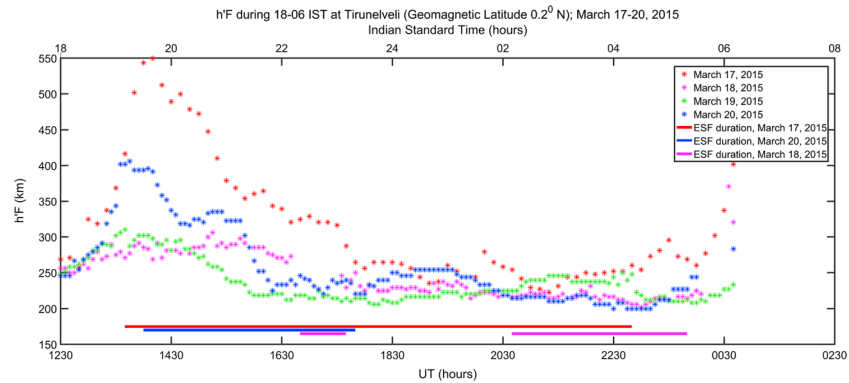


**Figure 2.** Virtual height  $h'F$  obtained from the digital ionosonde at dip equatorial station Tirunelveli during the post-sunset hours of 17–20 March 2015. Horizontal lines at the bottom of the figure show the duration of spread F as seen from ionograms of the respective days. IST = Indian Standard Time; ESF = equatorial spread F.

and 0600 IST on the next day is shown for 17–20 March 2015. As has been mentioned in several papers (Kakad et al., 2016; Ramsingh et al., 2015; Tulasi Ram et al., 2016), on 17 March, the second southward turning of the IMF  $B_z$  at around 12:30 UT caused a large eastward electric field of magnetospheric origin to penetrate into the equatorial ionosphere in the Indian longitude region at a time when disturbance dynamo effects arising from earlier geomagnetic activity may also have been present. This occurred around the time of the normal PRE of the eastward electric field in the equatorial F region. The net result of this was to increase  $h'F$  to ~550 km over the equatorial station TIR (Kakad et al., 2016; Ramsingh et al., 2015). On 18 March, presence of a westward DDEF during the post-sunset hours reduces the quiet time eastward electric field generally present at this time. Hence,  $h'F$  derived from the CADI at Tirunelveli remains below 300 km. As stated in the previous paragraph, on 19 March, disturbance dynamo effects during daytime are so weak that their signature cannot be discerned in the EEJ. However, post-sunset, on this day the DDEF is stronger and westward in direction such that the normal PRE of the quiet time eastward electric field is suppressed and as on 18 March,  $h'F$  derived from the CADI at Tirunelveli remains below 300 km.

In an earlier paper (Bhattacharyya et al., 2017), in order to identify ambient ionospheric conditions which influence the latitudinal distribution of L-band scintillations,  $h'F$  on 17 March was compared with that on 13 March 2015, which was a quiet day ( $\Sigma Kp = 11-$ ,  $A_p = 6$ ). In the present paper, ionospheric conditions on 13 March are compared with those on 20 March 2015, when DDEF and PPEF related to the 17 March storm seem to be absent in the equatorial ionosphere. In Figure 3a, AE index for 12 and 13 March 2015 are plotted for comparison with the AE index on 19 and 20 March 2015. Figure 3b displays the EEJ variations on 13 and 20 March. Finally, Figure 3c shows that the post-sunset increase of  $h'F$ , an important factor in the occurrence of an EPB, is nearly identical for these 2 days. Thus, larger values of AE index prior to the post-sunset hours of 20 March did not cause  $h'F$  on this day to be significantly different from that on 13 March, which was preceded by almost 24 hr of very low auroral activity. The peak  $h'F$  due to PRE of the eastward electric field on 20 March is lower than that on 13 March by about 10 km. As can be seen from Figure 3b, the EEJ was much stronger on 20 March as compared to 13 March, which could be due to promptly penetrated eastward electric field related to substorm activity and possibly enhanced conductivity due to higher electron density and an increase in ion-neutral collisions. Presence of a significant westward DDEF around the time of the PRE on 20 March due to large variations in AE index would have suppressed the normal PRE of the quiet time eastward electric field as on 19 March. However, it is possible that E-region conductivity gradients were affected by an increase in ion-neutral collisions on 20 March. This could lead to the peak  $h'F$  on 20 March to be lower than that on 13 March by about 10 km. The EUV solar flux levels for these 2 days are nearly the same as indicated by the F10.7 values on these 2 days, which were 117.9 and 111.8 for 13 and 20 March, respectively. These observations are used to characterize the ambient ionospheric conditions prevailing on these 2 days, as the objective of this paper is to compare the evolution of EPBs on these 2 days using scintillation measurements, which are described in the next section.

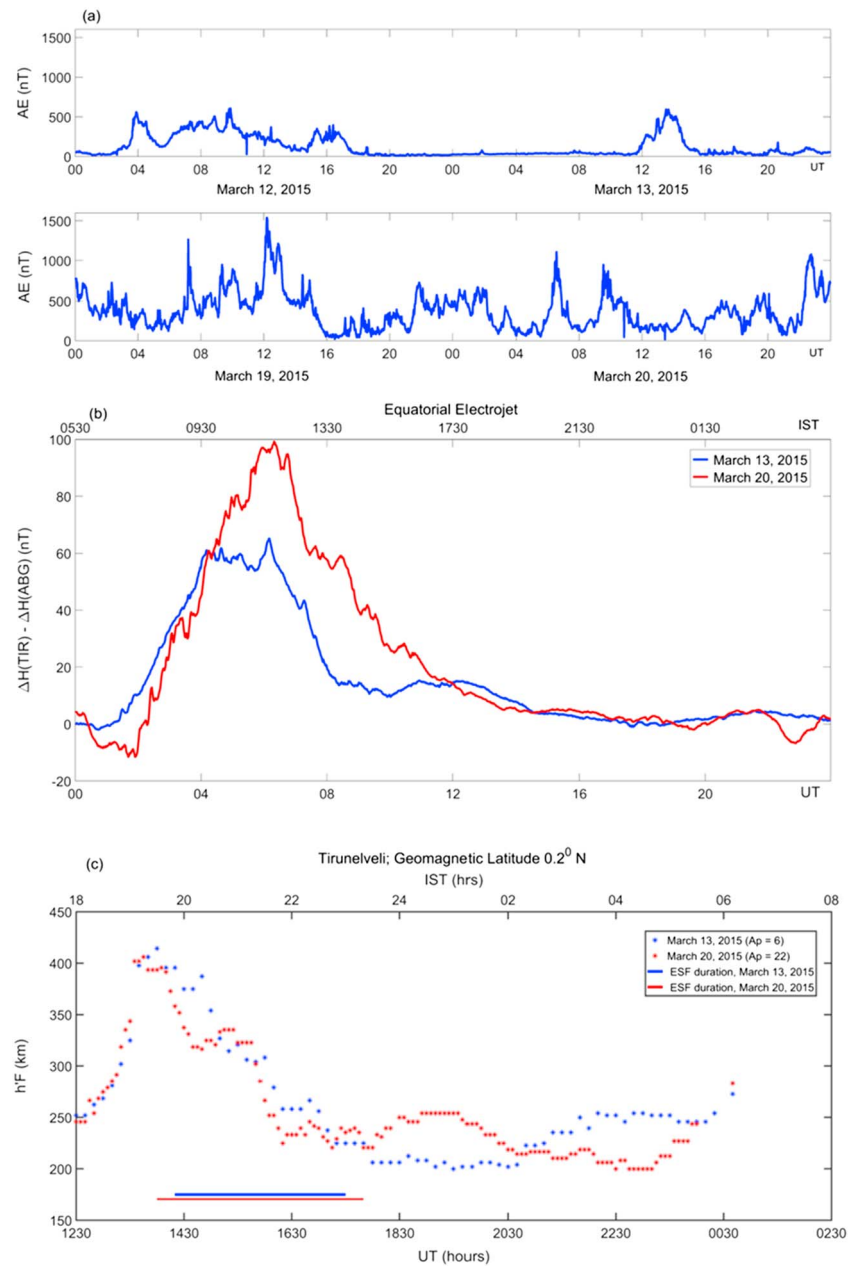


**Figure 3.** (a) Temporal variation of AE index on 12–13 March 2015 compared with that on 19–20 March 2015. (b) Variation of equatorial electrojet in the Indian longitude region on 13 and 20 March 2015. (c) Variation of  $h'F$  obtained at dip equatorial station Tirunelveli during the post-sunset hours of 13 and 20 March 2015. Horizontal lines at the bottom of the figure show the duration of spread F as seen from ionograms of the respective days. IST = Indian Standard Time.

### 3. Latitudinal Distribution of VHF and L-Band Scintillations

Scintillation data recorded by a network of VHF and L-band receivers are used to study the latitudinal distribution of VHF and L-band scintillations on 13 and 20 March 2015. Locations of these receivers are shown in Figure 4. Amplitude of a 251 MHz radio signal transmitted from geostationary satellite UFO10 located at 72.4°E is recorded by the four VHF receivers at time intervals of 0.05 s. Table 1 lists the geographic and geomagnetic coordinates of the ionospheric penetration points (IPPs) at an altitude of 300 km for the 251 MHz signal recorded at these four stations. The signal paths to the four VHF stations have the following zenith and azimuth (measured eastward from North) angles: TIR = 12° and 212°; KOP = 19.9° and 190.2°; MUM = 22.4° and 181.4°; and ALD = 31.7° and 202.8°. Figure 1b of Bhattacharyya et al. (2017) gives an



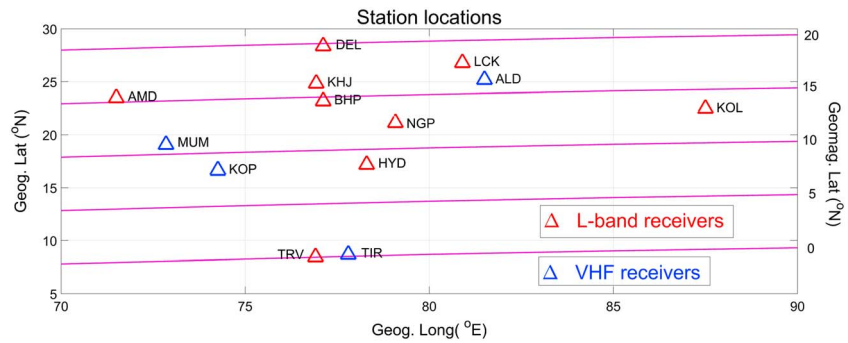


**Figure 4.** Locations of the stations with VHF and L-band receivers. Geomagnetic latitudes are displayed as mauve lines and the corresponding geomagnetic latitudes at 90°E longitude are marked on the right-hand side axis.

estimate of the altitude at the geomagnetic equator where irregularities must appear in the nonlinear phase of development of an EPB, in order to map down to the locations of IPPs at 300 km for off-equatorial stations. Scintillation data on an L1 signal (1.575 GHz) are obtained from nine stations. Of these, apart from Nagpur (NGP), remaining eight stations are part of the Indian SBAS (satellite-based augmentation system) network GAGAN (GPS Aided Geo Augmented Navigation). The  $S_4$ -index, which is the standard deviation of normalized intensity of the signal, generally used as a measure of the strength of amplitude scintillations, is computed for 3-min intervals from the VHF scintillation data. For L-band scintillations, signal intensity data for the L1 signal sampled at 50 Hz has been used to compute the  $S_4$ -index for 1-min intervals.

Latitudinal distribution of VHF scintillations on 13 and 20 March are compared in Figure 5. Figures 5a and 5b show that on 20 March, VHF scintillations were not recorded at ALD as the signal did not encounter any scintillation-producing irregularities whereas on 13 March such irregularities were encountered near the F layer peak, giving rise to scintillations with  $S_4$  of about 0.5 for nearly 30 min. The IPP for the VHF signal recorded at ALD is located at a geomagnetic latitude of 14.88°N. For the other three VHF stations, with IPPs extending up to about 10°N, scintillation strengths recorded on these 2 days are not significantly different although the duration of recorded VHF scintillations is shorter on 13 March as compared to 20 March. Absence of scintillations in ALD records on 20 March indicates that on this day, the maximum altitude where irregularities appeared at the dip equator was lower than that on 13 March. This is also the case with scintillations recorded on these 2 days on the L1 signal transmitted from geostationary satellite GSAT-10 (PRN 128) located at 83°E and recorded by the network of L-band receivers.

In Figure 6,  $S_4$ -indices computed from the GSAT-10 L1 signal recorded at different latitudes, for those intervals when the signal path elevation angle is not less than 55°, are plotted. It is evident from this figure that the latitudinal extent of L-band scintillations is smaller on 20 March than on 13 March. This supports the conclusion that the maximum height reached by EPBs at the dip equator on 20 March is lower than that on 13 March. In Figure 7, temporal changes in the spatial distribution of scintillations recorded on the L1 signal transmitted from all the other visible GNSS satellites, not in geostationary orbits, are shown for 13

and 20 March 2015. The data used in the plots are restricted to intervals when the signal path elevation angle is not less than 55°. Such plots are useful in understanding the evolution and dynamics of the EPBs. For improved clarity, average values of L1  $S_4$  computed for 5-min intervals have been plotted along the IPP tracks at 300 km altitude for each visible satellite whenever the signal path elevation angle  $\geq 55^\circ$ , with the size and color of the plotted circles representing different ranges of  $S_4$ . Comparison of Figures 7a and 7b shows that over the Indian longitude region, ionospheric irregularities that produce L-band scintillations appeared with a significant delay on 20 March as compared to 13 March, when moderate to strong L-band scintillations were recorded at geomagnetic latitudes between 10° and 15° during the interval 19–20 IST. As the EPBs rise and drift eastward along with associated irregularities, L-band scintillations intensify during 20–21 IST on both nights. Also, very weak or no L-band

**Table 1**

*Geographic and Geomagnetic Coordinates of the IPPs at an Altitude of 300 km for the 251 MHz Signal Paths From UFO10 to the VHF Receiver Locations*

Station	IPP geographic latitude	IPP geographic longitude	IPP geomagnetic latitude	IPP geomagnetic longitude
TIR	8.24°N	77.50°E	0.23°S	150.46°E
KOP	15.77°N	74.15°E	7.51°N	147.85°E
MUM	18.03°N	72.82°E	9.87°N	146.78°E
ALD	23.75°N	80.90°E	14.88°N	155.00°E

Note. IPP = ionospheric penetration point.

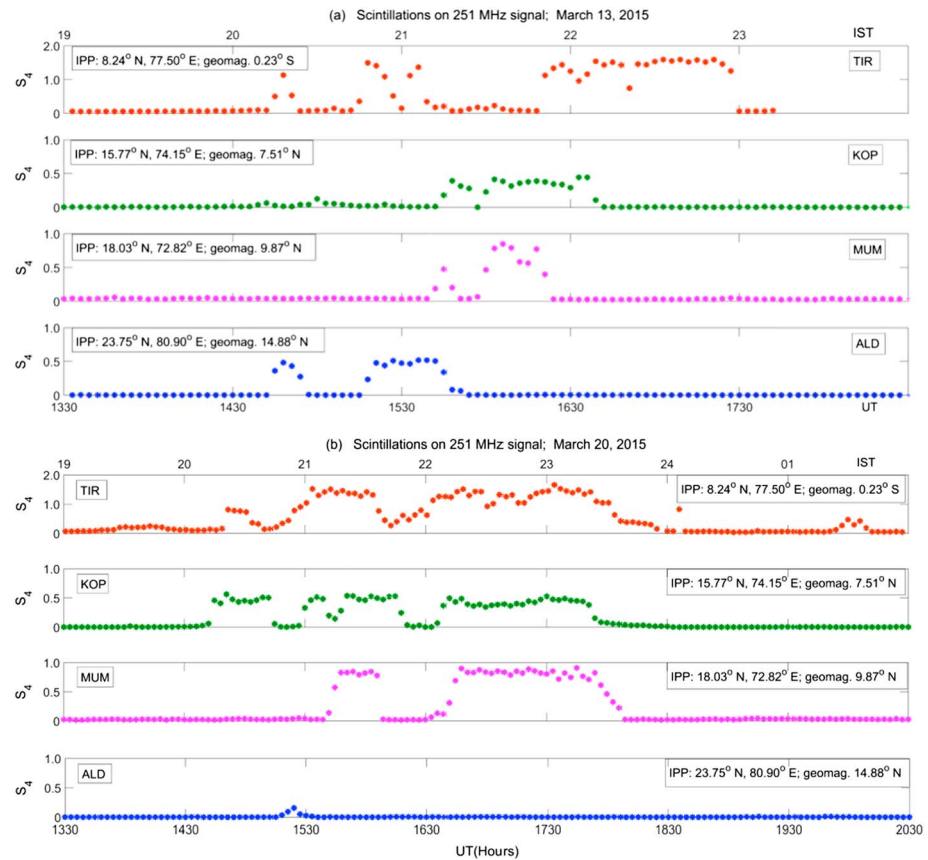


**Figure 5.** Variation of  $S_4$ -index with IST for scintillations on the 251 MHz signal transmitted from geostationary satellite UFO and recorded at all four VHF receiver stations on (a) 13 March 2015 and (b) 20 March 2015. Geographic coordinates and geomagnetic latitude of the IPPs of the signal paths at 300 km altitude, in each case, are indicated in the figures. IST = Indian Standard Time; IPP = ionospheric penetration point.

scintillations are recorded near the dip equator in both cases. Bhattacharyya et al. (2017) have attributed this to an EPB being more structured on the topside of the equatorial F layer than near the equatorial F region peak. Thus, irregularities that are capable of producing L-band scintillations are mapped from the equatorial topside to off-equatorial F-peak regions. On the other hand, near the equatorial F region peak, the intermediate scale irregularity spectrum is too steep to give rise to significant L-band scintillations.

On 13 March, L-band scintillations with  $S_4$  exceeding 0.5 are recorded for signal paths with IPPs at 300 km having a geomagnetic latitude of about  $15^\circ\text{N}$ , in the  $75\text{--}80^\circ\text{E}$  longitude zone. The irregularities at an altitude of 300 km producing these scintillations would map down from an altitude of about 780 km above the dip equator. On 20 March, no L-band scintillations were recorded for these signal paths. In fact, L-band scintillations were not recorded for signal paths with IPPs beyond  $11.5^\circ\text{N}$  in the  $75\text{--}80^\circ\text{E}$  longitude zone on 20 March. The irregularities at an altitude of 300 km and geomagnetic latitude  $11.5^\circ\text{N}$  that produce L-band scintillations would map down from an altitude of about 570 km above the dip equator. These observations suggest that over the dip equator, EPBs rose to an altitude of about 780 km on 13 March as compared to  $\sim 570$  km on 20 March. Also, Figure 7 shows that L-band scintillations were recorded on signal paths with IPPs in the  $85\text{--}90^\circ\text{E}$  longitude zone on 13 March, which is not the case on 20 March.

On the night of 18–19 March, scintillations were observed on the VHF signal recorded at the four VHF stations, only during post-midnight period (not shown here). These VHF scintillations were produced by irregularities generated elsewhere, which had drifted into the path of the received signals, and shorter scale irregularities required to produce scintillations on an L-band signal were not present as they would have decayed. Hence, no L-band scintillations were recorded on this night. On 19 March, neither L-band nor VHF scintillations were observed. As noted earlier, on 18 and 19 March, the PRE of the zonal eastward

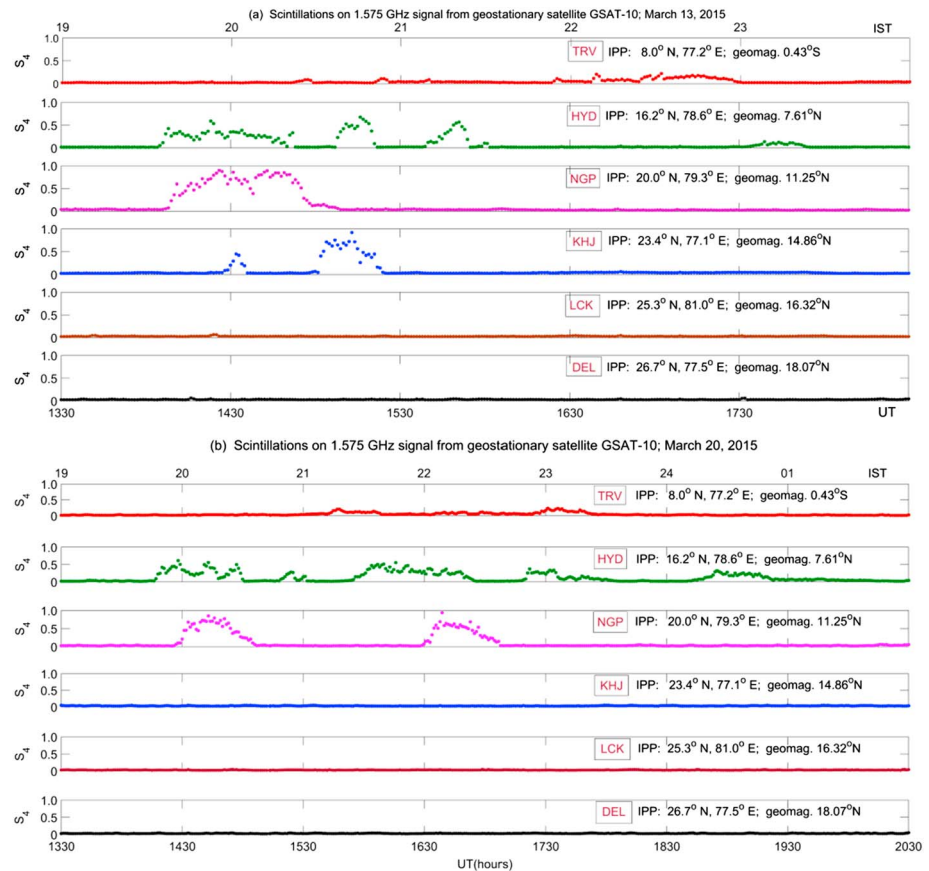


**Figure 6.** Variation of  $S_4$ -index with IST for scintillations on the 1.575 GHz signal transmitted from geostationary satellite GSAT-10 and recorded at L-band receiver stations on (a) 13 March 2015 and (b) 20 March 2015. For all the stations represented in this plot, the signal path elevation angle is not less than  $55^\circ$ . Geographic coordinates and geomagnetic latitude of the IPPs of the signal paths at 300 km altitude, in each case, are indicated in the figures. IST = Indian Standard Time; IPP = ionospheric penetration point.

electric field over the equatorial station Tirunelveli was opposed by westward DDEF, so that h'F for both these nights remained below 300 km. Therefore, absence of L-band scintillations on these two nights is in agreement with the past observations of the effect of height of the post-sunset equatorial F region on the growth and evolution of EPBs (Bhattacharyya et al., 2017; Fejer et al., 1999). However, heights of the equatorial F region during post-sunset hours on 13 and 20 March are not significantly different as can be seen from Figure 3c. Yet there is a marked difference in the latitudinal distribution of scintillations. The possibility of other ambient conditions influencing the evolution of EPBs is explored in the next section.

#### 4. Role of Ambient Conditions in Evolution of EPBs

Background plasma distributions in the region of interest on 13 and 20 March 2015 are compared in Figure 8, where vertical total electron content (VTEC), computed from GNSS signals recorded at five stations located at different geomagnetic latitudes in the  $76.9\text{--}79.1^\circ\text{E}$  longitudinal belt, are plotted for these 2 days. Once again, data used to estimate VTEC is restricted to those signal paths which have an elevation angle  $\geq 55^\circ$ . NGP station has a GNSS receiver while the other stations shown in Figure 8 have GPS receivers. Consequently many more signals are recorded at NGP than at the other stations, resulting in a noisy plot for NGP (second plot from bottom). Also at NGP station, during certain time intervals, all the signals received have an elevation angle less than  $55^\circ$ . This has caused the two data gaps seen in the second plot from bottom in Figure 8. As can be seen, temporal variation of VTEC on these 2 days is not very different at all locations except that at a geomagnetic latitude of  $16.27^\circ\text{N}$ , where VTEC is enhanced during 09–12 UT (14:30–17:30 IST) on 20 March as compared to 13 March 2015, possibly due to PPEF present at



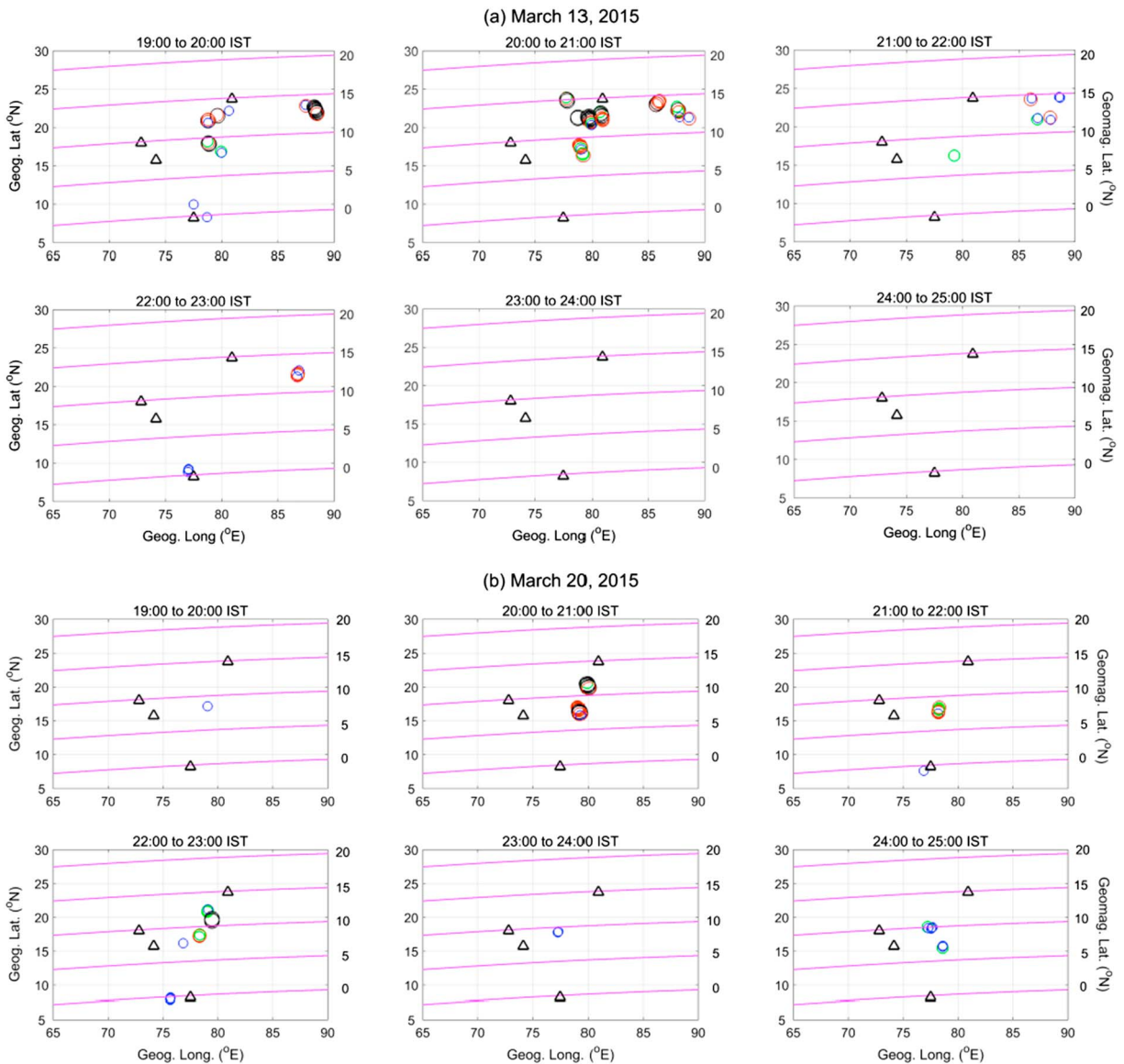


**Figure 7.** Spatial and temporal variation of L-band scintillations recorded for all visible GNSS satellites during periods when the signal path elevation angle is not less than  $55^\circ$ . Circles of different colors and sizes indicate the level of 5-min averages of L-band  $S_4$ -indices computed along the tracks of ionospheric penetration points at 300 km altitude for each satellite: (a) on 13 March 2015 and (b) on 20 March 2015. Four different levels of  $S_4$  are shown: (1) blue circles for  $0.15 \leq S_4 \leq 0.25$ ; (2) green circles for  $0.25 \leq S_4 \leq 0.35$ ; (3) red circles for  $0.35 \leq S_4 \leq 0.5$ ; (4) black circles for  $S_4 > 0.5$ . Locations of the ionospheric penetration points at 300 km altitude for the VHF signal recorded at the four VHF stations are marked by triangles. Geomagnetic latitudes are displayed as mauve lines with the corresponding geomagnetic latitudes at  $90^\circ\text{E}$  longitude marked on the right-hand side axis. IST = Indian Standard Time.

the dip equator a few hours earlier, which gave rise to a stronger EEJ on 20 March, as noted before. Around sunset, VTEC over the equatorial station, Tirunelveli, is nearly the same on 13 and 20 March 2015. Presence of EPBs is seen in the VTEC plots up to a geomagnetic latitude of  $8.58^\circ\text{N}$  on both nights. VTEC maps at 14 UT (19:30 IST) on both days, based on Global Ionospheric Maps generated by JPL, are shown in the top and middle panels of Figure 9. The box outlined in red shows the region between  $70\text{--}90^\circ\text{E}$  longitude and  $5\text{--}30^\circ\text{N}$  latitude, from where scintillation measurements have been used here. From the bottom panel of this figure, which shows the contours of the difference in VTEC at 19:30 IST on the 2 days, it is seen that at this hour, the difference between VTEC on 20 and 13 March at the locations of interest is within  $\pm 5$  total electron content unit,  $1 \text{ TECU} = 10^{16}$  electron per square meter. This observation together with the nearly same h'F around sunset on the 2 days

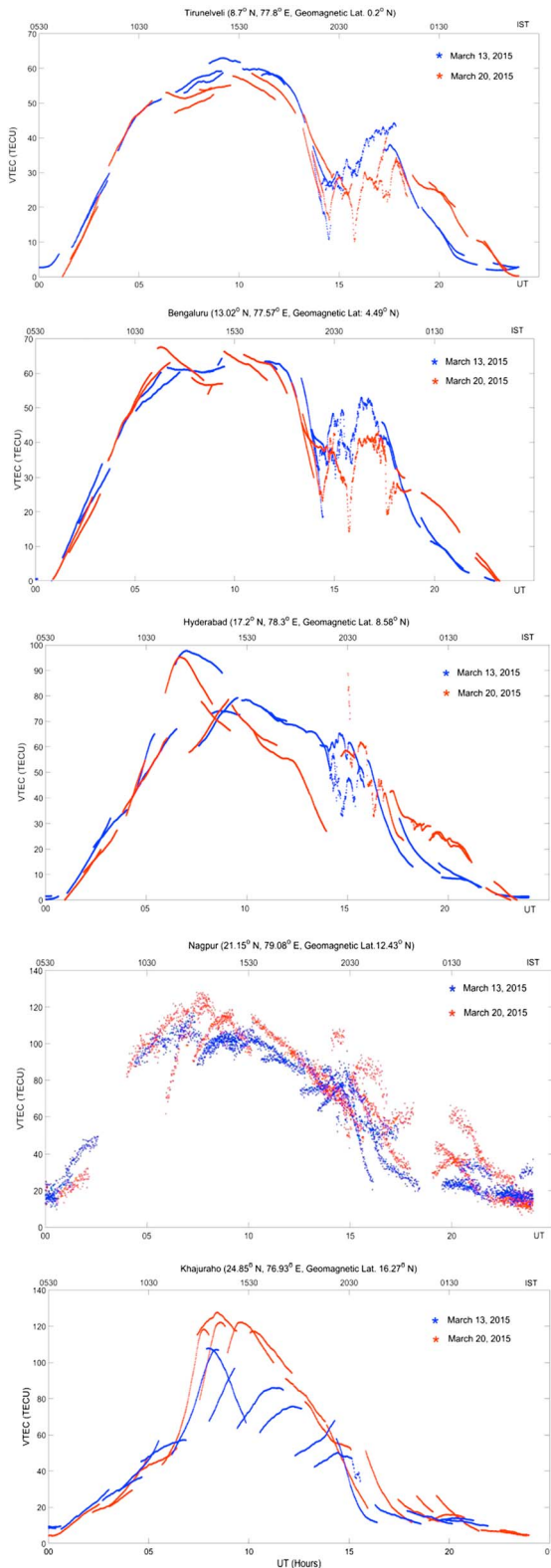


**Figure 8.** Temporal variation of VTEC on 13 and 20 March 2015 at a chain of stations extending in geomagnetic latitude from 0.2 to 16.3°N, in the geographic longitude range of 76.9–79.1°E. IST = Indian Standard Time; VTEC = vertical total electron content; TECU = total electron content unit, 1 TECU =  $10^{16}$  electron per square meter.

(Figure 3c) indicate that at 19:30 IST, the zonal electric field as well as thermospheric winds may not be significantly different on these 2 days.

Importance of the post-sunset height of the equatorial F region in the growth of the EPB arises from the role played by ion-neutral collisions in the growth of the R-T instability. As the ion-neutral collision frequency,  $\nu_{in}$ , decreases rapidly with height due to the nearly exponential decrease in neutral density, a higher altitude of the post-sunset bottomside equatorial F layer causes a more rapid growth of the R-T instability and hence of an EPB in the initial, linear phase. In the present study, emphasis is on the rise of EPBs and development of structure in EPBs, which happens in the nonlinear phase of evolution of an EPB when it also reaches the linearly stable topside of the equatorial F layer. In previous work (Bhattacharyya et al., 2017) it has been shown that as a result of the St. Patrick's Day magnetic storm, peak h'F after sunset on 17 March 2015 was 150 km higher than that on 13 March 2015. As a result, the maximum height that the EPBs reached above the geomagnetic equator on 17 March was about 300 km higher than that on 13 March. The height of the post-sunset bottomside equatorial F layer on 20 March is just 10 km lower than that on 13 March. This difference in peak h'F is not expected to give rise to a 210-km difference in the maximum height reached by the EPBs over the geomagnetic equator on the 2 days, if thermospheric conditions are the same on 13 and 20 March. However, a significant difference in the growth rate of the R-T instability can still arise if the neutral density at this height differs substantially on the 2 days. This is so because the ion-neutral collision frequency is proportional to the neutral density. With atomic oxygen as the dominant neutral component and  $O^+$  as the dominant ion species at the heights of interest, the ion-neutral collision frequency, in second inverse is given by (Schunk & Nagy, 2000)

$$\nu_{in} = 3.67 \times 10^{-11} n(O) T_r^{1/2} (1 - 0.064 \log_{10} T_r)^2, \quad (1)$$

where  $T_r = (T_i + T_n)/2$ ,  $T_i$  and  $T_n$  being the ion and neutral temperatures, respectively. Any changes in  $T_i$  and  $T_n$  would also contribute to variation in  $\nu_{in}$  between the 2 days. As discussed in the next section, the maximum height to which the EPBs rise above the dip equator may also be substantially affected due to this factor. This would result in different latitudinal distributions of VHF and L-band scintillations observed on the 2 days. Given the changes in the thermosphere caused by the geomagnetic storm of 17 March 2015 and subsequent magnetic activity, considerable differences in the thermosphere are expected between 13 and 20 March. In the absence of thermospheric data, thermospheric densities on these 2 days are compared on the basis of model calculations. The Coupled Thermosphere, Ionosphere, Plasmasphere, and Electrodynamics (CTIPE) model (Fuller-Rowell et al., 1996; Millward et al., 1996) is used for this purpose. This model has provided insights into various processes that determine the response of the thermosphere and ionosphere at different latitudes, to magnetic storms in their early and late phases (Fuller-Rowell et al., 2007; Fuller-Rowell, 2011). Of the four distinct components of CTIPE, which are fully coupled with respect to energy, momentum, and continuity, the thermospheric code yields the wind vector, temperature, and number density of the three major neutral species O, O<sub>2</sub>, N<sub>2</sub>, and mean molecular mass. High latitude convection electric field required as input to CTIPE is obtained from the Weimer (2005) model driven by solar wind parameters including the IMF. For

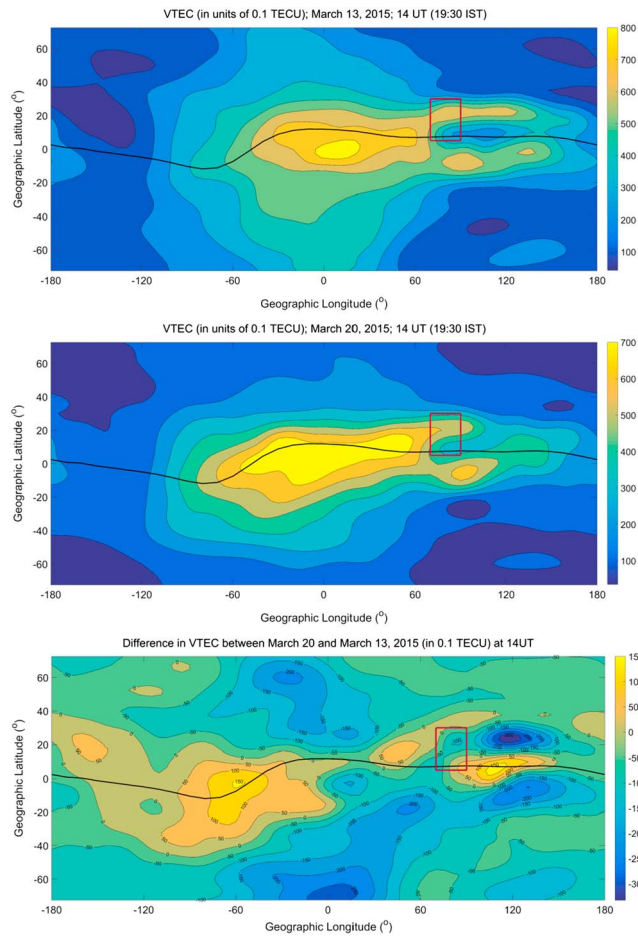


**Figure 9.** Distribution of VTEC at 14 UT (19:30 IST) on 13 March 2015 (top) and 20 March 2015 (middle). Distribution of the difference in VTEC between 20 and 13 March 2015 at 14 UT is shown in the bottom panel. Box outlined in red shows the region between 70–90°E longitude and 5–30°N latitude. Black curve is the dip equator. IST = Indian Standard Time; VTEC = vertical total electron content; TECU = total electron content unit, 1 TECU =  $10^{16}$  electron per square meter.

the 2015 CTIPE simulation results presented here, 1-min hemispheric power input is obtained from inferred values based on correlations of Advanced Composition Explorer measurements with NOAA POES hemispheric power data (Codrescu et al., 2012). For the thermospheric output, latitude resolution is  $2^\circ$ , longitude resolution is  $18^\circ$ , and in the vertical direction the output is available at 15 levels in logarithm of pressure from lower boundary of 1 Pa at about 80 km altitude. The neutral atmosphere density, composition, and wind response in CTIPE has been validated comprehensively for past storms (e.g., Codrescu et al., 2012; Fedrizzi et al., 2012; Fuller-Rowell et al., 2007, 2008; Negrea et al., 2012). Figure 10 shows the simulated number density of atomic oxygen at an altitude of 250 km at 14 UT on 13 and 20 March 2015. The low-latitude region in the Indian longitude zone is marked by the box outlined in blue in the figures. In this region, simulated atomic oxygen number density at an altitude of 250 km at 14 UT (19:30 IST) is about 13–22% higher on 20 March as compared to 13 March 2015. Simulated altitude profiles of atomic oxygen number density above the dip equator at  $77.8^\circ\text{E}$  at 14 UT on 13 and 20 March 2015 are shown in Figure 11a. The estimated number density of atomic oxygen is higher on 20 March as compared to 13 March throughout the range of heights shown in Figure 11a, with the difference decreasing with height. At a height of 420 km, the model values of atomic oxygen number density are  $3.53 \times 10^{13}$  and  $4.15 \times 10^{13} \text{ m}^{-3}$ , respectively, on 13 and 20 March, showing an increase of 17% in the post-storm period. Simulated ion and neutral temperature profiles for the 2 days are shown in Figure 11b. Changes in  $T_i$  and  $T_n$  are negligible. Ion neutral collision frequency profiles for 13 and 20 March computed using CTIPE results and equation (1) are shown in Figure 11c. Possible effect of the increase in  $\nu_{in}$  on 20 March as compared to 13 March on the development of EPBs is discussed in the next section.

## 5. Discussion

Results presented in the previous sections compare the ionospheric conditions prevailing on 2 days in March 2015: 13 March, which is a quiet day before the St. Patrick's Day magnetic storm of 17 March 2015, and 20 March, which is well into the recovery phase of the storm. Although 20 March is not entirely a quiet day, the EEJ at TIR on this

day shows no effects of the disturbance dynamo which was active on 18 and 19 March. The post-sunset conditions in the equatorial and low-latitude ionosphere on 20 March are also not significantly different from those prevailing on 13 March. Following the PRE of the eastward electric field present post-sunset, h'F over the dip equator at  $77.5^\circ\text{E}$  on both days reaches a maximum of about 400 km around the same time, and after the reversal of the zonal electric field to westward, the descent of the ionosphere also take place at a similar rate on both nights. Scintillations occur on both nights, on a 251 MHz signal transmitted from a geostationary satellite and recorded by three receivers for which the IPPs of the signal path have geomagnetic latitudes of 0.23, 7.51, and  $9.87^\circ\text{N}$  (see Table 1). However, for the fourth receiver, for which the IPP of the signal path is at  $14.88^\circ\text{N}$ , moderate VHF scintillations are recorded only on 13 March, with the  $S_4$ -index maintaining a value of about 0.5 for approximately 30 min. From Figure 5 it is seen that VHF scintillations recorded at the equatorial station (TIR) and also the off-equatorial stations (KOP and MUM) last longer by at least an hour on 20 March as compared to 13 March, which indicates that favorable conditions for growth may have existed further west of the observing locations on 20 March, and the EPBs generated there continued to drift eastward and came into the path of the VHF signals received at TIR, KOP, and MUM at a later time on 20 March thus increasing the duration of recorded scintillations at these locations in comparison with 13 March. With the available data, it is only possible to compare the ionospheric conditions over the equatorial region in the neighborhood of  $77.5^\circ\text{E}$  longitude on 13 and 20



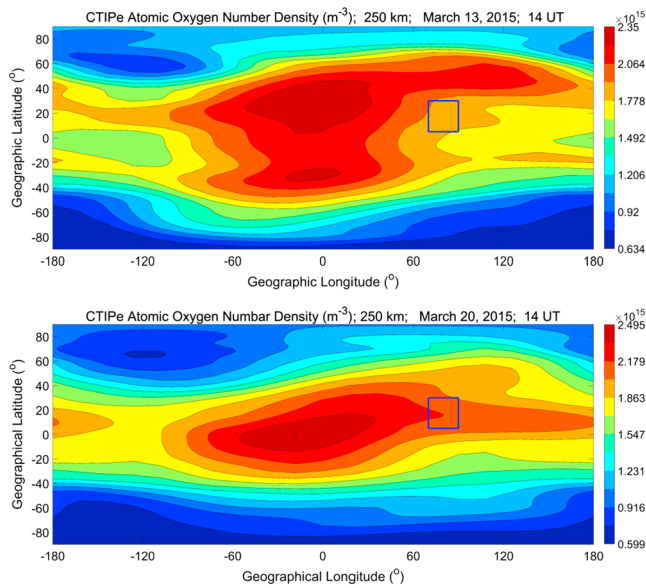


**Figure 10.** CTIPe simulated distribution of atomic oxygen number density at an altitude of 250 km at 14 UT (19:30 IST) on 13 March 2015 (top) and 20 March 2015 (bottom). Box outlined in blue shows the region between 70–90°E longitude and 5–30°N latitude. CTIPe = Coupled Thermosphere, Ionosphere, Plasmasphere, and Electrodynamics.

March. Hence in this paper, the focus is on the latitudinal distribution of scintillations around this longitude. It is clear from Figure 5 that on 20 March EPBs generated over the dip equator after sunset, in the 72–81°E longitude region, did not reach an altitude of about 770 km in the equatorial region. Thus, the irregularities did not map to an altitude of 300 km at a geomagnetic latitude of 14.88°N in this longitude zone. This is the location of the IPP for the 251 MHz signal recorded at station ALD, where no VHF scintillations were observed on 20 March. This result is corroborated by observations from a network of L-band receivers. IPPs of the signals from various satellites recorded by the L-band receivers give a good coverage of the region.

It is to be noted that maximum contribution to the observed amplitude scintillations comes from the region of the peak of the F layer where  $\Delta N$  would be the largest due to the maximum in background electron density. Figure 6 shows that L-band scintillations are insignificant at the dip equatorial location on 13 March as well as 20 March, although strong VHF scintillations were recorded here on both nights. It has been suggested that this commonly observed phenomenon may be due to the EPB over the dip equator being more structured on the topside than near the equatorial F-peak (Bhattacharyya et al., 2017). This would imply that a few hundred meter scale size irregularities responsible for producing L-band scintillations are only present in the equatorial topside where the background electron density is low. These equatorial topside irregularities

map down to the F region peak at off-equatorial latitudes. There is also a latitudinal gradient in the background electron density due to the presence of the equatorial ionization anomaly on both days. This also contributes to L-band scintillations being stronger at a geomagnetic latitude of 11.25°N than at 7.61°N on both the days. IPP for the higher latitude station (NGP) is only 0.76° east of that for the lower latitude station (HYD). However, on both days, L-band scintillations occurred first at the lower latitude station. Occurrence of L-band scintillation-producing irregularities at 300 km altitude at a geomagnetic latitude of 7.61°N requires that an EPB reaches the height of about 420 km above the dip equator. For these irregularities to occur at the same height at a geomagnetic latitude of 11.25°N would require that the EPB reaches a height of about 560 km above the dip equator. This may introduce a delay of a few minutes in the initial occurrence of scintillations at the northern location (NGP) as seen on 20 March. At a later time, scintillations observed at this location would be due to irregularities drifting in from the west. It is clear from Figure 6 that on 13 March the EPBs encountered by the signal recorded at the lower latitude station, HYD, produced the second and third patches of L-band scintillations recorded here. However, these EPBs did not reach a height of 560 km above the dip equator. Consequently, they did not map down to the IPP for the northern station NGP. The same holds for the last two patches of scintillations recorded at HYD on 20 March. Most importantly, on 13 March, the signal from GSAT-10 encounters irregularities of a few hundred meter scale size, at an altitude of ~300 km at a geomagnetic latitude of 14.86°N. On 20 March, no such irregularities are present around this location to cause scintillations on the L-band signal recorded at the station KHJ. The picture becomes clearer in Figure 7. Here the presence of irregularities that produce L-band scintillations on GPS/GNSS signals recorded at a network of receivers are displayed at corresponding IPP locations at 300 km altitude for different time intervals. Late evolution of irregularities of few hundred meters scale size in the 75–80°E longitudinal belt on 20 March as compared to 13 March is evident in this figure. While such irregularities are present at a geomagnetic latitude of about 15°N on 13 March, they are not present beyond a geomagnetic latitude of 11.5°N on 20 March. Thus, the EPBs associated with the irregularities attained a height of ~780 km above the dip equator on 13 March, whereas they only rose to a height of ~570 km above the dip equator on 20 March.

In an earlier paper (Bhattacharyya et al., 2017), vertical extent of EPBs above the dip equator was found to increase significantly with an increase in the post-sunset h'F. In the present case, it has been noted that post-sunset h'F is nearly the same for 13 and 20 March 2015. Thus, it is necessary to consider other factors that

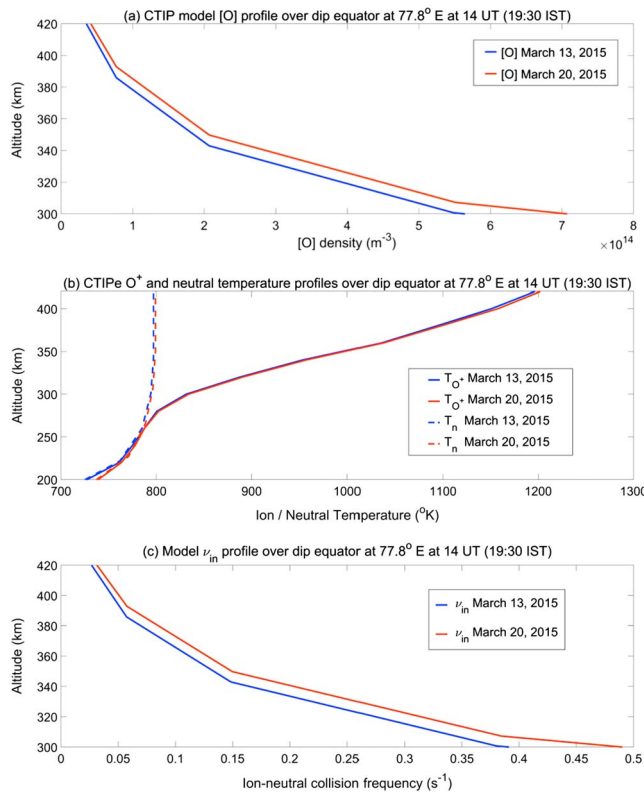


**Figure 11.** CTIPE simulated altitude profiles of (a) atomic oxygen number density and (b) ion and neutral temperatures; above the dip equator at 77.8°E at 14 UT on 13 and 20 March 2015. (c) Profiles of ion-neutral collision frequency above the dip equator at 77.8°E at 14 UT on 13 and 20 March 2015 computed using the CTIPE simulation results. CTIPE = Coupled Thermosphere, Ionosphere, Plasmasphere, and Electrodynamics; IST = Indian Standard Time.

control the vertical extent of an EPB above the dip equator. According to a linear theory (Ossakow & Chaturvedi, 1978), the magnitude of the initial rise velocity of an EPB over the dip equator is given by

$$V = \frac{\Delta N}{N_0} \left( \frac{g}{\nu_{in}} + \frac{cE_0}{B} \right), \quad (2)$$

where  $\Delta N/N_0$  is the magnitude of fractional depletion of plasma density inside the EPB,  $\nu_{in}$  is the ion-neutral collision frequency,  $E_0$  is an ambient eastward electric field, and  $B$  is the geomagnetic field. In this equation  $g$  is the acceleration due to gravity and  $c$  is the velocity of light. This expression indicates that on a day with a significantly higher concentration of atomic oxygen over the dip equator, resulting in a higher  $\nu_{in}$ , the initial EPB rise velocity may be smaller. However, to seek an answer to the question of when an EPB stops rising, simulation of the nonlinear evolution of EPBs has to be carried out. Krall et al. (2010) have reported the results of such a study using the Naval Research Laboratory three-dimensional code SAMI3/ESF. They found that EPBs stop rising when the magnetic flux tube-integrated ion mass density inside the bubble equals that of the surrounding background ionosphere. The background ionosphere itself is not static and starts descending once the equatorial electric field becomes westward. For 2 days with similar rate of descent of the background ionosphere from the same maximum height, the height at which an EPB stops rising may still be different. On the day with a smaller rise velocity of an EPB, the magnetic flux tube-integrated ion mass density inside the bubble would equal that of the surrounding background ionosphere when the EPB is at a lower height. Thus, the EPB would stop rising at a lower height compared to the other day. This scenario may explain the difference in the maximum height attained by EPBs on 13 March 2015, which is a magnetically quiet day and on 20 March 2015. On 20 March, concentration of atomic oxygen was significantly larger as a result of magnetic activity in the preceding days.

## 6. Conclusion

Recent efforts to explain the day-to-day variability in the observations of L-band scintillations at equatorial and low-latitude stations (e.g., Carter, Yizengaw, et al., 2014, Carter, Retterer, Yizengaw, Groves, et al., 2014, Carter, Retterer, Yizengaw, Wiens, et al., 2014) have been based on a flux tube-integrated linear growth rate of the R-T instability (Sultan, 1996). In these studies, TIEGCM has been used to model the ionosphere-thermosphere and estimate the parameters that appear in the linear growth rate of the R-T instability. From these investigations, the PRE of the upward plasma drift of the equatorial F region has emerged as the most important driver of the day-to-day variability in EPB occurrence. In many studies of the effect of geomagnetic storms on EPB occurrence, it has been found that presence of a promptly penetrated zonal electric field or such an electric field arising from a disturbance dynamo associated with magnetic activity are factors that control the occurrence of EPBs. However, there have been no studies of the effect of thermospheric conditions on the nonlinear evolution of EPBs. In the present paper it is shown that observations of L-band scintillations at off-equatorial locations cannot be explained only on the basis of the linear growth rate of the R-T instability on the bottomside of the equatorial ionosphere. Thermospheric changes in the dip equatorial region during the recovery phase of a magnetic storm may significantly affect the evolution of EPBs. It is found that changes in the concentration of atomic oxygen, the dominant neutral species present in the F region, in the aftermath of a storm, affects the maximum height to which an EPB rises. In the case study presented here, 2 days are considered with nearly the same background ionospheric conditions. On a day with significantly enhanced concentration of atomic oxygen, resulting in an increased ion-neutral collision frequency, not only is the growth rate of an EPB impacted but more importantly the maximum height to which an EPB can



rise is curtailed. This is directly linked with the occurrence of L-band scintillations at off-equatorial latitudes.

#### Acknowledgments

Thanks are due to K.U. Nair, Ananthi, Rupesh, P. Tiwari, and S. Banola for their technical support in the VHF scintillation experiment at Indian Institute of Geomagnetism (IIG), Department of Science and Technology, Government of India. The World Data Centre for Geomagnetism at Kyoto University (<http://wdc.kugi.kyoto-u.ac.jp/>) is acknowledged for providing the geomagnetic activity indices. The global ionospheric maps (GIM) are available online (<ftp://cddis.gsfc.nasa.gov/gps/products/ionex/>). Geomagnetic data for Tirunelveli and Alibag are available at the World Data Centre for Geomagnetism, Mumbai (<http://wdciig.res.in>). Ionosonde data, VHF and L-band scintillation data, and CTIPE results are available online (<https://doi.org/10.5281/zenodo.2548591>). A. B. acknowledges the Indian National Science Academy for an INSA senior scientist position and director IIG for hosting the position at IIG. S.S. acknowledges the support of the Airport Authority of India.

#### References

- Abdu, M. A. (2012). Equatorial spread F/plasma bubble irregularities under storm time disturbance electric fields. *Journal of Atmospheric and Solar - Terrestrial Physics*, 75–76, 44–56.
- Abdu, M. A., Batista, I. S., Takahashi, H., MacDougall, J., Sobral, J. H., Medeiros, A. F., & Trivedi, N. B. (2003). Magnetospheric disturbance induced equatorial plasma bubble development and dynamics: A case study in Brazilian sector. *Journal of Geophysical Research*, 108(A12), 1449. <https://doi.org/10.1029/2002JA009721>
- Anderson, D. N., Anghel, A., Yumoto, K., Ishitsuka, M., & Kudeki, E. (2002). Estimating daytime, vertical E<sub>B</sub> drift velocities in the equatorial F-region using ground-based magnetometer observations. *Geophysical Research Letters*, 29(12), 1596. <https://doi.org/10.1029/2001GL014562>
- Anghel, A., Anderson, D., Maruyama, N., Chau, J., Yumoto, K., Bhattacharyya, A., & Alex, S. (2007). Interplanetary electric fields and their relationship to low-latitude electric fields under disturbed conditions. *Journal of Atmospheric and Solar - Terrestrial Physics*, 69, 1147–1159. <https://doi.org/10.1016/j.jastp.2006.08.018>
- Basu, S., Basu, S., MacKenzie, E., Bridgwood, C., Valladares, C. E., Groves, K. M., & Carrano, C. (2010). Specification of the occurrence of equatorial ionospheric scintillations during the main phase of large magnetic storms within solar cycle. *Radio Science*, 45, RS5009. <https://doi.org/10.1029/2009RS004343>
- Basu, S., Basu, S., Rich, F. J., Groves, K. M., MacKenzie, E., Coker, C., et al. (2007). Response of the equatorial ionosphere at dusk to penetration electric fields during intense magnetic storms. *Journal of Geophysical Research*, 112, A08308. <https://doi.org/10.1029/2006JA012192>
- Bhattacharyya, A. (2004). Role of E region conductivity in the development of equatorial ionospheric plasma bubbles. *Geophysical Research Letters*, 31, L06806. <https://doi.org/10.1029/2003GL018960>
- Bhattacharyya, A., Basu, S., Groves, K. M., Valladares, C. E., & Sheehan, R. (2002). Effect of magnetic activity on the dynamics of equatorial F region irregularities. *Journal of Geophysical Research*, 107(A12), 1489. <https://doi.org/10.1029/2002JA009644>
- Bhattacharyya, A., Groves, K. M., Basu, S., Kuenzler, H., Valladares, C. E., & Sheehan, R. (2003). L-band scintillation activity and space-time structure of low-latitude UHF scintillations. *Radio Science*, 38(1), 1004. <https://doi.org/10.1029/2002RS002711>
- Bhattacharyya, A., Kakad, B., Gurrani, P., Sripathi, S., & Sunda, S. (2017). Development of intermediate-scale structure at different altitudes within an equatorial plasma bubble: Implications for L-band scintillations. *Journal of Geophysical Research: Space Physics*, 122, 1015–1030. <https://doi.org/10.1002/2016JA023478>
- Carter, B. A., Retterer, J. M., Yizengaw, E., Groves, K., Caton, R., McNamara, L., et al. (2014). Geomagnetic control of equatorial plasma bubble activity modeled by the TIEGCM with Kp. *Geophysical Research Letters*, 41, 5331–5339. <https://doi.org/10.1002/2014GL060953>
- Carter, B. A., Retterer, J. M., Yizengaw, E., Wiens, K., Wing, S., Groves, K., et al. (2014). Using solar wind data to predict daily GPS scintillation occurrence in the African and Asian low-latitude regions. *Geophysical Research Letters*, 41, 8176–8184. <https://doi.org/10.1002/2014GL062203>
- Carter, B. A., Yizengaw, E., Pradipta, R., Retterer, J. M., Groves, K., Valladares, C., et al. (2016). Global equatorial plasma bubble occurrence during the 2015 St. Patrick's Day storm. *Journal of Geophysical Research: Space Physics*, 121, 894–905. <https://doi.org/10.1002/2015JA022194>
- Carter, B. A., Yizengaw, E., Retterer, J. M., Francis, M., Terkildsen, M., Marshall, R., et al. (2014). An analysis of the quiet time day-to-day variability in the formation of postsunset equatorial plasma bubbles in the southeast Asian region. *Journal of Geophysical Research: Space Physics*, 119, 3206–3223. <https://doi.org/10.1002/2013JA019570>
- Chakrabarty, D., Sekar, R., Narayanan, R., Patra, A. K., & Devasia, C. V. (2006). Effects of interplanetary electric field on the development of an equatorial spread F event. *Journal of Geophysical Research*, 111, A12316. <https://doi.org/10.1029/2006JA011884>
- Codrescu, M. V., Negrea, C., Fedrizzi, M., Fuller-Rowell, T. J., Dobin, A., Jakowsky, N., et al. (2012). A real-time run of the coupled thermosphere ionosphere plasmasphere electrodynamics (CTIPE) model. *Space Weather*, 10, S02001. <https://doi.org/10.1029/2011SW000736>
- Fedrizzi, M., Fuller-Rowell, T. J., & Codrescu, M. V. (2012). Global Joule heating index derived from thermospheric density physics-based modeling and observations. *Space Weather*, 10, S03001. <https://doi.org/10.1029/2011SW000724>
- Fejer, B. (2002). Low latitude storm time ionospheric electrodynamics. *Journal of Atmospheric and Solar - Terrestrial Physics*, 64, 1401–1408. [https://doi.org/10.1016/S1364-6826\(02\)00103-7](https://doi.org/10.1016/S1364-6826(02)00103-7)
- Fejer, B., & Scherliess, L. (1997). Empirical model of storm-time equatorial zonal electric fields. *Journal of Geophysical Research*, 102, 24,047–24,056. <https://doi.org/10.1029/97JA02164>
- Fejer, B. G., Scherliess, L., & de Paula, E. R. (1999). Effects of the vertical plasma drift velocity on the generation and evolution of equatorial spread F. *Journal of Geophysical Research*, 104, 19,859–19,869. <https://doi.org/10.1029/1999JA000271>
- Fuller-Rowell, T., Codrescu, M., Maruyama, N., Fedrizzi, M., Araujo-Pradere, E., Sazykin, S., & Bust, G. (2007). Observed and modeled thermosphere and ionosphere response to superstorms. *Radio Science*, 42, RS4S90. <https://doi.org/10.1029/2005RS003392>
- Fuller-Rowell, T. J. (2011). Storm-time response of the thermosphere-ionosphere system. In M. A. Abdu, D. Pancheva, & A. Bhattacharyya (Eds.), *Aeronomy of the Earth's atmosphere and ionosphere, IAGA Special Sopron Series* (Vol. 2, pp. 419–435). Dordrecht, Netherlands: Springer Science+Business Media B.V. [https://doi.org/10.1007/978-94-007-0326-1\\_32](https://doi.org/10.1007/978-94-007-0326-1_32)
- Fuller-Rowell, T. J., Rees, D., Quegan, S., Moffet, R. J., Codrescu, M. V., & Millward, G. H. (1996). A coupled thermosphere ionosphere model (CTIM). In R. W. Schunk (Ed.), *Handbook of ionospheric models, STEP report* (pp. 217–238). Logan: Utah State University.
- Fuller-Rowell, T. J., Richmond, A., & Maruyama, N. (2008). Global modeling of storm time thermospheric dynamics and electrodynamics. In P. M. Kintner, Jr., A. J. Coster, T. J. Fuller-Rowell, A. J. Mannucci, M. Mendillo, & R. Heelis (Eds.), *Midlatitude ionospheric dynamics and disturbances, Geophysical Monograph Series* (Vol. 181, pp. 187–200). Washington, DC: American Geophysical Union. <https://doi.org/10.1029/181GM18>
- Groves, K. M., Basu, S., Weber, E. J., Smitham, M., Kuenzler, H., Valladares, C. E., et al. (1997). Equatorial scintillation and systems support. *Radio Science*, 32, 2047–2064. <https://doi.org/10.1029/97RS00836>
- Huang, C.-S., Wilson, G. R., Hairston, M. R., Zhang, Y., Wang, W., & Liu, J. (2016). Equatorial ionospheric plasma drifts and O<sup>+</sup> concentration enhancements associated with disturbance dynamo during the 2015 St. Patrick's Day magnetic storm. *Journal of Geophysical Research: Space Physics*, 121, 7961–7973. <https://doi.org/10.1002/2016JA023072>

- Jiang, C., Yang, G., Liu, J., Yokoyama, T., Liu, T., Lan, T., et al. (2017). Equatorial and low-latitude ionospheric response to the 17–18 March 2015 great storm over Southeast Asia longitude sector. *Journal of Geophysical Research: Space Physics*, *122*, 5756–5767. <https://doi.org/10.1002/2017JA024134>
- Kakad, B., Gurram, P., Tripura Sundari, P. N. B., & Bhattacharyya, A. (2016). Structuring of intermediate scale equatorial spread F irregularities during intense geomagnetic storm of solar cycle 24. *Journal of Geophysical Research: Space Physics*, *121*, 7001–7012. <https://doi.org/10.1002/2016JA022635>
- Kakad, B., Jeeva, K., Nair, K. U., & Bhattacharyya, A. (2007). Magnetic activity linked generation of nighttime equatorial spread F irregularities. *Journal of Geophysical Research*, *112*, A07311. <https://doi.org/10.1029/2006JA012021>
- Kil, H., Lee, W. K., Paxton, L. J., Hairston, M. R., & Jee, G. (2016). Equatorial broad plasma depletions associated with the evening pre-reversal enhancement and plasma bubbles during the 17 March 2015 storm. *Journal of Geophysical Research: Space Physics*, *121*, 10,209–10,219. <https://doi.org/10.1002/2016JA023335>
- Krall, J., Huba, J. D., Ossakow, S. L., & Joyce, G. (2010). Why do equatorial ionospheric bubbles stop rising? *Geophysical Research Letters*, *37*, L09105. <https://doi.org/10.1029/2010GL043128>
- Kuai, J., Liu, L., Liu, J., Sripathi, S., Zhao, B., Chen, Y., et al. (2016). Effects of disturbed electric fields in the low latitude and equatorial ionosphere during the 2015 St. Patrick's Day storm. *Journal of Geophysical Research: Space Physics*, *121*, 9111–9126. <https://doi.org/10.1002/2016JA022832>
- Li, G. B., Ning, L., Hu, L., Liu, X., Yue, W., Wan, B., et al. (2010). Longitudinal development of low-latitude ionospheric irregularities during the geomagnetic storms of July 2004. *Journal of Geophysical Research*, *115*, A04304. <https://doi.org/10.1029/2009JA014830>
- Martinez, C. R., Mendillo, M. J., & Aarons, J. (2005). Toward a synthesis of equatorial spread F onset and suppression during geomagnetic storms. *Journal of Geophysical Research*, *110*, A07306. <https://doi.org/10.1029/2003JA010362>
- Millward, G. H., Moffett, R. J., Quegan, S., & Fuller-Rowell, T. J. (1996). A coupled thermosphere ionosphere plasmasphere model (CTIP). In R. W. Schunk (Ed.), *Handbook of ionospheric models, STEP report* (pp. 239–279). Logan: Utah State University.
- Mullen, J. P., Mackenzie, E., Basu, S., & Whitney, H. (1985). UHF/GHz scintillation observed at Ascension Island from 1980 through 1982. *Radio Science*, *20*, 357–365. <https://doi.org/10.1029/RS020i003p00357>
- Nava, B., Rodríguez-Zuluaga, J., Alazo-Cuartas, K., Kashcheyev, A., Migoya-Orué, Y., Radicella, S. M., et al. (2016). Middle- and low-latitude ionosphere response to 2015 St. Patrick's Day geomagnetic storm. *Journal of Geophysical Research: Space Physics*, *121*, 3421–3438. <https://doi.org/10.1002/2015JA022299>
- Nayak, C., Tsai, L.-C., Su, S.-Y., Galkin, I. A., Tan, A. T. K., Nofri, E., & Jamjareegularn, P. (2016). Peculiar features of the low-latitude and midlatitude ionospheric response to the St. Patrick's Day geomagnetic storm of 17 March 2015. *Journal of Geophysical Research: Space Physics*, *121*, 7941–7960. <https://doi.org/10.1002/2016JA022489>
- Negrea, C., Codrescu, M. V., & Fuller-Rowell, T. J. (2012). On the validation effort of the coupled thermosphere ionosphere plasmasphere electrodynamics model. *Space Weather*, *10*, S08010. <https://doi.org/10.1029/2012SW000818>
- Ossakow, S. L., & Chaturvedi, P. K. (1978). Morphological studies of rising equatorial spread F bubbles. *Journal of Geophysical Research*, *83*, 2085–2090. <https://doi.org/10.1029/JA083iA05p02085>
- Ramsingh, S., Sripathi, S., Sreekumar, S., Banola, K., Emperumal, P. T., & Kumar, B. S. (2015). Low-latitude ionosphere response to super geomagnetic storm of 17/18 March 2015: Results from a chain of ground-based observations over Indian sector. *Journal of Geophysical Research: Space Physics*, *120*, 10,864–10,882. <https://doi.org/10.1002/2015JA021509>
- Rastogi, R. G., & Klobuchar, J. A. (1990). Ionospheric electron content within the equatorial f2 layer anomaly belt. *Journal of Geophysical Research*, *95*, 19,045–19,052. <https://doi.org/10.1029/JA095iA11p19045>
- Ray, S., Roy, B., Paul, K. S., Goswami, S., Oikonomou, C., Haralambous, H., et al. (2017). Study of the effect of 17–18 March 2015 geomagnetic storm on the Indian longitudes using GPS and C/NOFS. *Journal of Geophysical Research: Space Physics*, *122*, 2551–2563. <https://doi.org/10.1002/2016JA023127>
- Scherliess, L., & Fejer, B. G. (1997). Storm time dependence of equatorial disturbance dynamo zonal electric fields. *Journal of Geophysical Research*, *102*, 24,037–24,046. <https://doi.org/10.1017/CBO9780511551772>
- Schunk, R. W., & Nagy, A. F. (2000). *Ionospheres: Physics, plasma physics, and chemistry*. Cambridge, UK: Cambridge University Press.
- Sripathi, S., Bose, S., Patra, A. K., Pant, T. K., Kakad, B., & Bhattacharyya, A. (2008). Simultaneous observations of ESF irregularities over Indian region using radar and GPS. *Annales de Geophysique*, *26*, 3197–3213. <https://doi.org/10.5194/angeo-26-3197-2008>
- Sultan, P. J. (1996). Linear theory and modeling of the Rayleigh-Taylor instability leading to the occurrence of equatorial spread F. *Journal of Geophysical Research*, *101*, 26,875–26,891. <https://doi.org/10.1029/96JA00682>
- Tulasi Ram, S., Rama Rao, P. V. S., Prasad, D. S. V. D., Niranjan, K., Gopi Krishna, S., Sridharan, R., & Ravindran, S. (2008). Local time dependent response of postsunset ESF during geomagnetic storms. *Journal of Geophysical Research*, *113*, A07310. <https://doi.org/10.1029/2007JA012922>
- Tulasi Ram, S., Yokoyama, T., Otsuka, Y., Shiokawa, K., Sripathi, S., Veenadhari, B., et al. (2016). Duskside enhancement of equatorial zonal electric field response to convection electric fields during the St. Patrick's Day storm on 17 March 2015. *Journal of Geophysical Research: Space Physics*, *121*, 538–548. <https://doi.org/10.1002/2015JA021932>
- Weimer, D. R. (2005). Improved ionospheric electrodynamic models and application to calculating Joule heating rates. *Journal of Geophysical Research*, *110*, A05306. <https://doi.org/10.1029/2004JA010884>
- Zhou, Y.-L., Lüher, H., Xiong, C., & Pfaff, R. F. (2016). Ionospheric storm effects and equatorial plasma irregularities during the 17–18 March 2015 event. *Journal of Geophysical Research: Space Physics*, *121*, 9146–9163. <https://doi.org/10.1002/2016JA023122>